ADVANCED OPTICAL MATERIALS

www.advopticalmat.de

Phase-Change-Material-Based Low-Loss Visible-Frequency Hyperbolic Metamaterials for Ultrasensitive Label-Free Biosensing

Kandammathe Valiyaveedu Sreekanth, Qingling Ouyang, Sivaramapanicker Sreejith, Shuwen Zeng, Wu Lishu, Efe Ilker, Weiling Dong, Mohamed ElKabbash, Yu Ting, Chwee Teck Lim, Michael Hinczewski, Giuseppe Strangi, Ken-Tye Yong, Robert E. Simpson,* and Ranjan Singh**

Hyperbolic metamaterials (HMMs) have emerged as a burgeoning field of research over the past few years as their dispersion can be easily engineered in different spectral regions using various material combinations. Even though HMMs have comparatively low optical loss due to a single resonance, the noble-metal-based HMMs are limited by their strong energy dissipation in metallic layers at visible frequencies. Here, the fabrication of noble-metal-free reconfigurable HMMs for visible photonic applications is experimentally demonstrated. The low-loss and active HMMs are realized by combining titanium nitride (TiN) and stibnite (Sb_2S_3) as the phase change material. A reconfigurable plasmonic biosensor platform based on active Sb_2S_3–TiN HMMs is proposed, and it is shown that significant improvement in sensitivity is possible for small molecule detection at low concentrations. In addition, a plasmonic apta-biosensor based on a hybrid platform of graphene and Sb_2S_3–TiN HMM is developed and the detection and real-time binding of thrombin concentration as low as 1×10^{-15} M are demonstrated. A biosensor operating in the visible range has several advantages including the availability of sources and detectors in this region, and ease of operation particularly for point-of-care applications.

The extreme anisotropic permittivity of hyperbolic metamaterials (HMMs) represent a unique opportunity to realize effective bulk metastructures with extraordinary optical properties over a broad frequency range from visible to terahertz.[1] HMMs are artificial uniaxial materials that exhibit hyperbolic dispersion because the out of plane dielectric constant ($\varepsilon_{zz} = \varepsilon_{\perp}$) has an opposite sign to the in-plane dielectric constants ($\varepsilon_{xx} = \varepsilon_{yy} = \varepsilon_{//}$). HMMs can be classified into two types based on the sign of their dielectric components, i.e., type I ($-\varepsilon_{\perp}$ and $\varepsilon_{//}$) and type II ($\varepsilon_{\perp}$ and $-\varepsilon_{//}$). In comparison to isotropic materials showing elliptical dispersion, HMMs support propagation of optical modes across the structure with infinitely large momentum (high-k modes) in the effective medium limit,[2,3] irrespective of

Dr. K. V. Sreekanth, W. Lishu, Prof. Y. Ting, Prof. R. Singh
Division of Physics and Applied Physics
School of Physical and Mathematical Sciences
Nanyang Technological University
Singapore 637371, Singapore
E-mail: ranjans@ntu.edu.sg

Dr. K. V. Sreekanth, Prof. R. Singh
Centre for Disruptive Photonic Technologies
The Photonics Institute
Nanyang Technological University
Singapore 637371, Singapore

Q. Ouyang, Prof. K.-T. Yong
School of Electrical and Electronic Engineering
Nanyang Technological University
Singapore 639798, Singapore
E-mail: ktyong@ntu.edu.sg

Q. Ouyang, Dr. S. Zeng
CINTRA CNRS/NTU/THALES
UMI 3288
Research Techno Plaza
Nanyang Technological University
50 Nanyang Drive, Singapore 637553, Singapore

Dr. S. Sreejith, Prof. C. T. Lim
Biomedical Institute for Global Health Research and Technology
National University of Singapore
Singapore 117599, Singapore

Dr. M. ElKabbash, Dr. E. Ilker, Prof. M. Hinczewski, Prof. G. Strangi
Department of Physics
Case Western Reserve University
10600 Euclid Avenue, Cleveland, OH 44106, USA

W. Dong, Prof. R. E. Simpson
Singapore University of Technology and Design
8 Somapah Road, Singapore 487372, Singapore
E-mail: robert_simpson@sutd.edu.sg

Prof. C. T. Lim
Department of Biomedical Engineering
National University of Singapore
Singapore 117583, Singapore

Prof. G. Strangi
Department of Physics and CNR-NANOTEC UOS of Cosenza
Licryl Laboratory
University of Calabria
87036 Rende, Italy

The ORCID identification number(s) for the author(s) of this article can be found under https://doi.org/10.1002/adom.201900081.

DOI: 10.1002/adom.201900081

the free space wavelength. Therefore, the high-*k* modes associated with HMMs can only be excited using a momentum coupler.[3–5] Since HMMs show extraordinary properties, they have been proposed for various applications.[6–18] By contrast, metamaterial designs rely on lithographic patterning, HMMs can easily be fabricated using conventional thin film physical vapor deposition techniques by depositing thin metal–dielectric multilayers in the effective medium regime. In order to realize hyperbolic dispersion over the frequency range from visible to terahertz, various metal–dielectric combinations have been proposed.[1–18]

Hyperbolic dispersion in the visible spectrum is particularly important for various applications, which has been usually achieved using the combination of gold or silver and dielectric such as SiO_2 or Al_2O_3 or TiO_2. Indeed, the noble-metal-based HMMs are severely limited due to the strong energy dissipation in noble metals at visible wavelengths. Since titanium nitride (TiN) is a potential low loss plasmonic material for visible and near-infrared (NIR) frequencies,[19] optical hyperbolic metamaterials with TiN as a plasmonic component have been proposed.[20] In addition, active HMMs have been proposed using tunable material such as graphene,[21] topological insulators,[22] hexagonal boron nitride,[23,24] and phase change materials (PCMs).[25–27] However, such tunable material-based HMMs show hyperbolic dispersion in the infrared and terahertz frequencies, and the visible frequency active HMMs[26,27] proposed so far have been based on the combination of noble metals and PCMs. A critical issue of noble metal–PCM-based active HMMs is the interdiffusion of noble metals (gold and silver) with phase change chalcogenides.[26–29] Therefore, the development of low-loss and diffusion-free active HMMs for the visible frequency range is important for active color filters for displays, adaptive camouflage systems, and biosensors. In particular, PCMs maintain their structural state and only require energy during the switching process, and this programmability can offer a lower energy consumption in comparison to liquid crystal and most mechanically tuned photonic devices, which require a constant energy supply.

Recently, label-free plasmonic biosensing with an extreme sensitivity has been achieved using HMMs,[15–17] which can detect small biomolecules at low concentrations. Kabashin et al. proposed to use HMMs in biosensing,[15] which was a type I HMM consisting of an assembly of electrochemically grown gold nanorods. More recently, a type II HMM for biosensing has been proposed by Sreekanth et al., it consisted of a multistack of gold/Al_2O_3 bilayers and the high-*k* modes were excited by grating coupling method.[16] In addition, the integration of 2D nanomaterials such as graphene with aptamers has emerged highly sensitive apta-biosensors for clinical diagnosis and food safety.[30] Apta-sensors use aptamers such as single standard oligonucleotides (DNA or RNA) as the molecular recognition elements, which are exhibited many advantages compared to traditional biosensors based on antibodies.[31–33] In particular, apta-biosensors are a good candidate for small molecule detection since the size of the aptamers are smaller than the antibodies. Therefore, the development of an apta-biosensor platform based on graphene and HMM can be used to improve the detection limit of small biomolecules.

Here, we propose and experimentally demonstrate a novel multilayered active HMM for reconfigurable biosensor applications. Our designed HMM is tunable, diffusion-free and low-loss, which supports type I hyperbolic dispersion at optical frequencies. This is realized by choosing appropriate number of alternating layers of stibnite (Sb_2S_3) and TiN thin films. Here, Sb_2S_3 acts as an active dielectric layer of the HMM that introduces reconfigurability as it is a low-loss PCM. We demonstrate the active properties of HMMs by switching the phase of the Sb_2S_3 from amorphous to crystalline. Stibnite is a wide bandgap PCM that exhibits a large change in the absorption edge at visible frequencies. Moreover, we report the experimental demonstration of the excitation of HMM guided mode as well as enhanced tunable Goos–Hänchen (GH) shift in the visible, at a wavelength of 632.8 nm, using a prism coupling scheme. Since the GH shift is a significant interrogation parameter for sensing applications, we use the GH shift to demonstrate tunable refractive index sensing and real-time biosensing of small biomolecules such as D-biotin (molecular weight = 244 Da) at a low concentration of 1×10^{-12} M. We further demonstrate the detection and real-time binding of thrombin concentration as low as 1×10^{-15} M by using a thrombin binding aptamer (TBA) functionalized hybrid graphene/ Sb_2S_3–TiN HMM.

The proposed low-loss and tunable Sb_2S_3–TiN HMM consists of ten alternating thin layers of Sb_2S_3 and TiN on a glass substrate. PCMs have received a great deal of attention in the research area of active photonic devices.[34] The main reason behind the selection of this multilayer combination is that many of the $Ge_2Sb_2Te_5$ (GST) tunable structures are not viable due to interdiffusion of noble metals with chalcogenides, when noble metals are in direct contact with chalcogenides.[35] Unlink the PCM GST, Sb_2S_3 has a bandgap of 2 eV, which renders it transmissive in the visible spectrum. Moreover, the dielectric function of Sb_2S_3 exhibits a substantial change in the visible frequencies when the structure of the material is switched from amorphous to crystalline phase.[36,37] To avoid diffusion problems typical of noble metals, TiN has been selected as a plasmonic component in the designed HMM. The cross-sectional scanning electron microscopy (SEM) image of fabricated Sb_2S_3–TiN HMM is shown in **Figure 1**a (also see Figure S1, Supporting Information). The sharp TiN–Sb_2S_3 interfaces confirm that there is no diffusion of TiN into Sb_2S_3. Figure 1b illustrates the proposed Sb_2S_3–TiN HMM-based biosensor platform.

As an initial study, the optical constants of Sb_2S_3 (in amorphous and crystalline phase) and TiN thin films were determined using spectroscopic ellipsometry (see Figure S2, Supporting Information). The real permittivity values of Sb_2S_3 exhibit a substantial change at visible frequencies when the phase of the material is switched from amorphous to crystalline, while the imaginary permittivity is very small for wavelengths greater than 500 nm for both phases. Therefore, Sb_2S_3 is an appropriate low loss and tunable dielectric material for the realization of active photonic devices and HMMs at visible frequencies. Note that the commonly used GST-based chalcogenides are very lossy in the visible frequencies (see Figure S8, Supporting Information). Therefore, unsuitable for visible HMM devices. It is clear from Figure S2c of the Supporting Information that TiN shows low-loss plasmonic behavior above 545 nm as the real permittivity values are negative and imaginary values

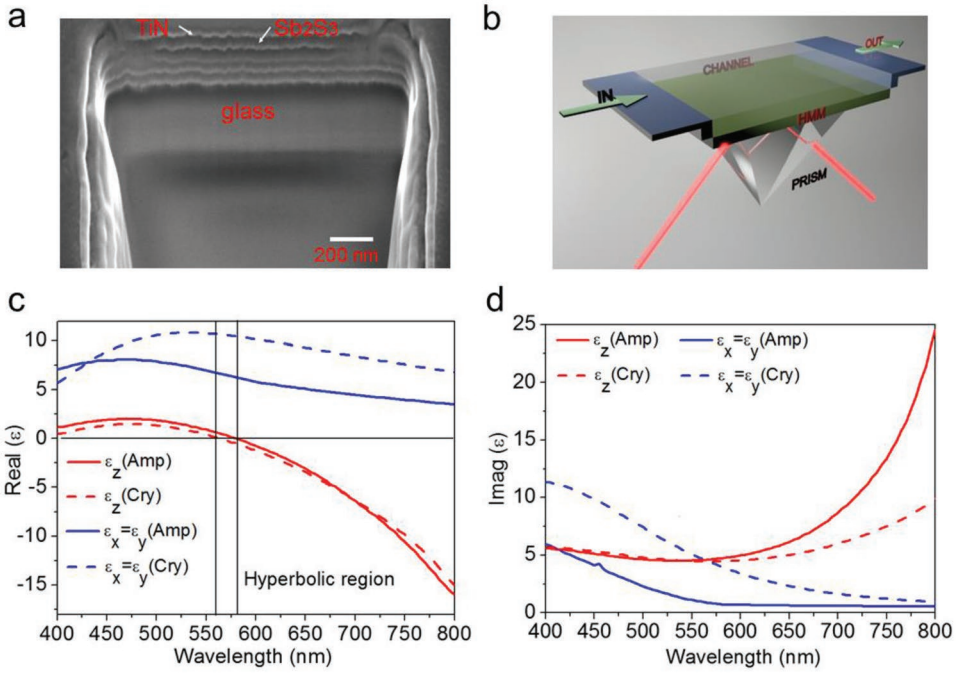

Figure 1. Development of visible-frequency active HMMs. a) A cross-sectional SEM image of the fabricated Sb_2S_3–TiN HMM consisting of five pairs of Sb_2S_3 and TiN, with a thickness of 25 nm Sb_2S_3 and 16 nm TiN. b) Schematic diagram of PDMS channel integrated prism coupled-HMM sensor device. Uniaxial permittivity components of Sb_2S_3–TiN HMM when Sb_2S_3 is in the amorphous and crystalline phases. c) Real parts and d) imaginary parts. HMM shows type I hyperbolic dispersion at $\lambda \geq 580$ nm and $\lambda \geq 564$ for amorphous and crystalline phase of Sb_2S_3, respectively.

are comparatively low. The HMM was fabricated by means of RF and DC sputtering (see Supporting Information). Thin film thicknesses were determined using spectroscopic ellipsometry and acquired thicknesses were around 25 and 16 nm for Sb_2S_3 and TiN, respectively. In the "as-deposited HMM samples," the Sb_2S_3 layers are amorphous (see Figure S3, Supporting Information). In order to switch the phase of the Sb_2S_3 from amorphous to crystalline, the HMM was baked at 300 °C for 30 min since the crystallization temperature[37] of Sb_2S_3 was determined to be above 285 °C.

Since the unit cell thickness of the fabricated HMM is much smaller than (λ/10) at the corresponding operating frequency, effective medium theory (EMT) was used to obtain the uniaxial permittivity.[2] The EMT-derived uniaxial permittivity components of multilayered Sb_2S_3–TiN HMM when Sb_2S_3 in amorphous and crystalline phases are shown in Figure 1c,d. According to Figure 1c, HMM shows type I hyperbolic dispersion at $\lambda \geq 580$ nm when Sb_2S_3 is in amorphous phase, where $\varepsilon_\perp = \varepsilon_z < 0$ and $\varepsilon_{ll} = \varepsilon_x = \varepsilon_y > 0$. However, the operating wavelength of type 1 region is slightly blue shifted to 564 nm wavelength after crystallizing the HMM. We further characterized the fabricated HMMs by studying reflectance and transmission spectra using variable angle spectroscopic ellipsometry. The acquired reflectance spectra at oblique incidence and transmission spectra at normal incidence are shown in Figures S4a,c and S5a of the Supporting Information, respectively. A red shift in reflectance dips and transmission peaks are observed after switching the phase of the Sb_2S_3 from amorphous to crystalline. The observed redshift in spectra is due to the increase of dielectric constants of Sb_2S_3 after crystallization.

A subwavelength periodic metal–dielectric stack (HMM) supports high wavevector guided modes, which are the entire family of gap plasmon modes of a multilayered HMM. Since these modes have high momentum, they can only be excited using a momentum coupler such as prism and grating. Until now, prism-coupling is used to excite HMM guided modes at NIR frequencies because the momentum matching condition is satisfied by use of a high-index silicon prism.[3] However, exciting HMM guided modes at visible frequencies is challenging because the high index prisms that are transparent in the visible are unavailable. Nevertheless, here we use prism coupling scheme to excite the guided modes of multilayered type I HMMs at visible frequencies since type I HMM has low-loss compared to type II HMM because of one negative permittivity component and it supports both low-*k* and high-*k* modes.[1] A custom-built angular surface plasmon resonance (SPR) spectroscopy set-up was used for this purpose (see Supporting Information). The excitation mechanism is based on the Kretschmann configuration, which includes a right-angle BK7 prism coupler. Transverse magnetic (TM) polarized light with a wavelength 632.8 nm was used as the excitation source because this wavelength belongs to the hyperbolic region of the HMM where its effective index is less than the prism index (see Figure S14b, Supporting Information), so that the incoming beam has sufficient momentum to match the momentum of the HMM guided modes.

Experimentally obtained reflectance spectra of Sb_2S_3–TiN HMM when Sb_2S_3 in both phases are shown in **Figure 2**a. The excitation of the guided mode is recognized as the angle at which minimum reflected intensity occurs and this minimum

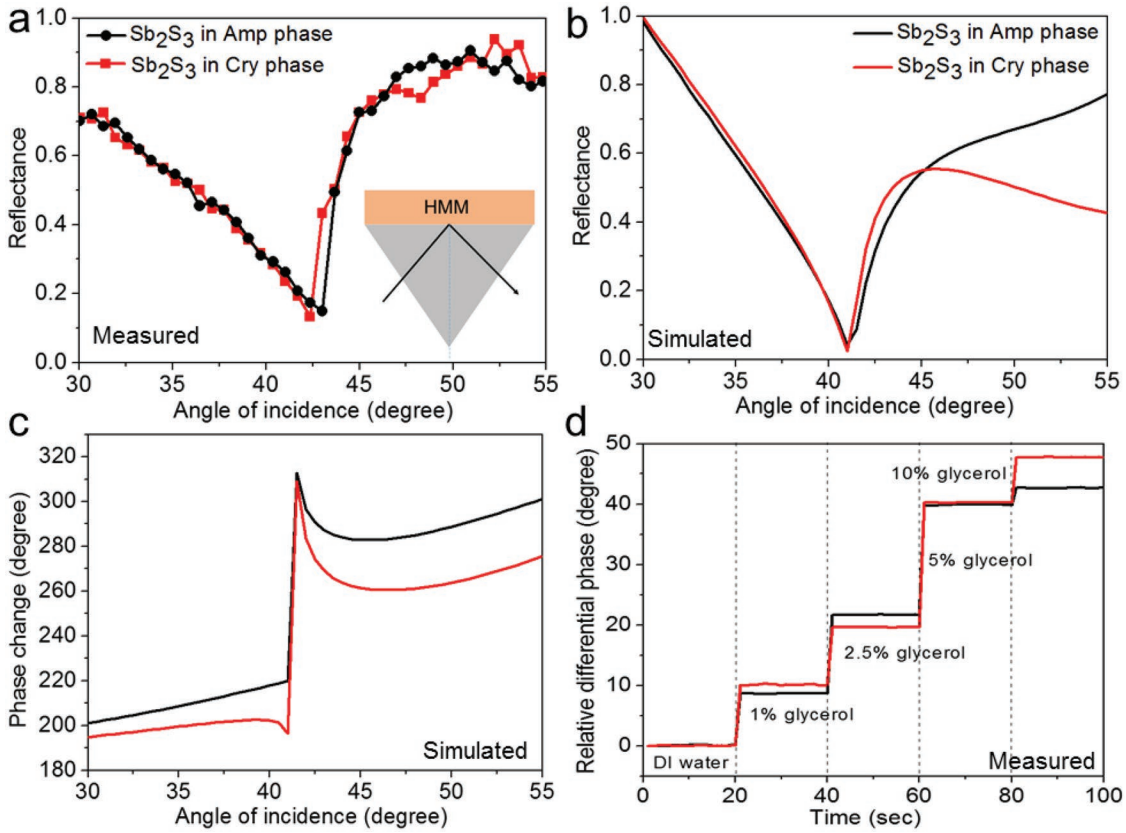

Figure 2. Excitation of HMM guided modes and differential phase change measurements. a) Experimentally obtained reflectance spectrum of Sb_2S_3–TiN HMM for both phases of Sb_2S_3. b) Corresponding simulated reflectance spectrum for both phases of Sb_2S_3. c) Simulated phase difference between TM and TE polarization as a function of incident angle. d) Real-time differential phase measurement for different weight ratios of glycerol in distilled water. A tunable phase difference was obtained in (c) and (d) by switching the phase of the Sb_2S_3 from amorphous to crystalline.

angle has been considered as the coupling (resonance) angle. We noticed that the minimum reflected intensity and linewidth of the spectrum decreased by switching the phase of the Sb_2S_3 from amorphous to crystalline state, which results in higher phase difference between TM and transverse electric (TE) polarized light for crystalline HMM. We simulated the reflectance and phase difference spectra of the HMM using the transfer matrix method (TMM), which is shown in Figure 2b,c, respectively. The simulated reflectance spectrum is qualitatively agreed with experimental results. In addition, a decrease in coupling angle is obtained after switching Sb_2S_3 phase from amorphous to crystalline. This is due to the decrease in effective index with phase change of Sb_2S_3 (see Figure S14b, Supporting Information). To further confirm that the excited mode is the unique guided mode of Sb_2S_3–TiN HMM, several control experiments, dispersion analysis, pointing vector calculation and supporting simulations were performed using different samples (see Supporting Information). It should be noted that the excited guided mode is the fundamental low-k bulk plasmon polariton mode of Sb_2S_3–TiN HMM (see Figures S14a and S15, Supporting Information).

The phase difference between TM and TE polarized light experiences a sharp singularity at the coupling angle of SPR reflectance spectrum.[38] As shown in Figure 2c, this phase difference could be actively tuned by switching the phase of the Sb_2S_3. We then experimentally confirmed this tunable phase difference by varying the external dielectric constant, which is shown in Figure 2d. A home-built differential phase-sensitive SPR setup was used for this purpose (see Figure S17, Supporting Information). One can clearly see that the relative differential phase increases with increase in glycerol concentration and a tunability in phase difference is possible by switching the phase of the Sb_2S_3 from amorphous to crystalline. Since there is a large phase variation at the coupling angle for both phases, an enhanced Goos–Hänchen shift is possible at those angles.

As experimentally demonstrated by Goos and Hänchen[39] in 1947, the GH shift is a lateral beam displacement of the reflected light from the interface of two media when the angles of incidence are very close to the critical angle. However, the direct observation of GH shift is very challenging because the shift, which is proportional to penetration depth, is normally of the order of the operating wavelength. Therefore, different approaches have been demonstrated to enhance both positive and negative GH shifts, such as using structural resonances,[40] absorptive materials,[41] photonic crystals,[42] and negative refractive index media.[43] As theoretical and numerical analyses of GH shift in a multilayered HMM have been previously investigated,[44–47] in this work, we show the experimental demonstration of enhanced GH shift in multilayered type I HMMs as well as tunable GH shifts. The basic principle of the origin of

enhanced GH shift in the case of prism-coupled HMM systems is the same as that of typical SPR system.[48] Once the phase matching condition is satisfied through the prism, the guided mode of the HMM can be excited at the prism–HMM interface, which is represented by the minimum reflectivity angle. A singularity in phase difference will happen at the coupling angle. Subsequently, the excited guided mode will propagate through the HMM and reflect out of the prism, which in turn generates a large lateral shift between incident and reflected beam. In particular, the phase derivative at the coupling angle determines the magnitude of GH shift.

An important advantage of using the HMM in the prism-coupled configuration for enhancing the GH shift is that the z-component of the wavevector (k_z) of the HMM can be modulated using the unique anisotropic property of HMM structure.[44] The k_z component becomes real or imaginary depending upon the sign of the uniaxial permittivity values ($\varepsilon_{\perp}$ and $\varepsilon_{//}$) of the HMM and the incident angle. According to the stationary phase approach, a general formula for calculating GH shift is given by[49] $S = -\frac{1}{k}\frac{\partial \phi}{\partial \theta}$ with k being the wavevector of the incident medium and ϕ being the reflected phase. The calculated GH shift of the proposed prism-coupled HMM system is shown in **Figure 3**a. One can see that maximum GH shift is obtained at the coupling angle where there is a sharp change of phase difference. It is shown that GH shift can also be tuned by switching the phase of the Sb_2S_3. This tunable behavior is experimentally verified in below. In another aspect, the enhanced GH shift in HMMs is due to the existence of Brewster mode in the HMM.[47]

Since the GH shift strongly depends on the substrate dielectric constant,[50,51] we developed a sensor platform based on the proposed prism-coupled HMM system. The configuration used for sensing purposes is shown in Figure 1b essentially, a polydimethylsiloxane (PDMS) channel with dimension $0.7 \times 0.7 \times 0.2$ cm^3 was attached to the prism coupled HMM system. For the GH shift measurements, a home-built differential phase-sensitive set up was used.[51,52] As a first step, the sensor device was calibrated by performing the bulk refractive index sensing, which was done by injecting different weight ratios (1% to 10% w/v) of aqueous solutions of glycerol with known refractive indices. The refractive index change was recorded by measuring the GH shift with time, which is shown for Sb_2S_3 in both structural phases in Figure 3b. We report a clear step function in GH shift by varying the glycerol concentrations and tunable GH shift by switching Sb_2S_3 from amorphous to crystalline phase state. The GH shift change with refractive index of the solution for amorphous and crystalline HMM samples are shown in Figure 3c,d, respectively. We

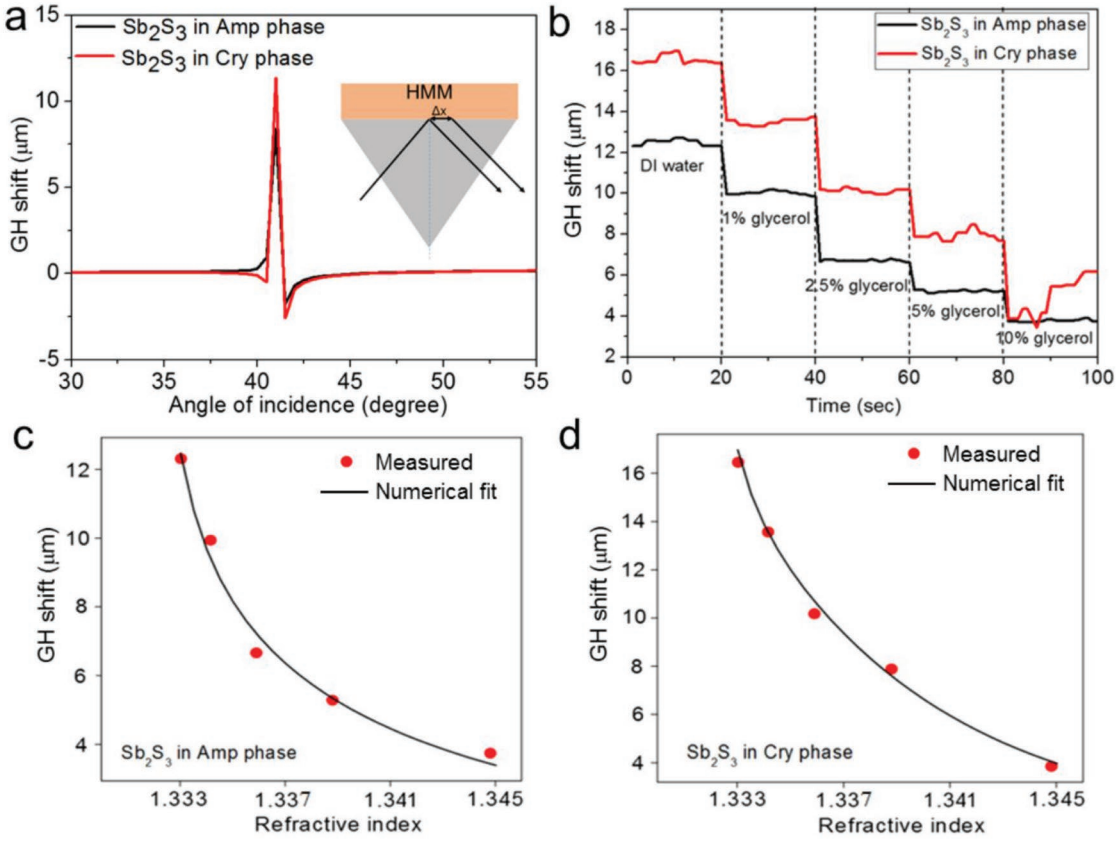

Figure 3. Sensor calibration using Goos–Hänchen shift interrogation scheme. a) Numerically calculated GH shift of a prism-HMM-air system, for both phases of HMM. b) Response of the sensor device by injecting different weight percentage concentration of glycerol in distilled water. Significant variation in GH shift was obtained when the glycerol weight percentage was increased from 1% to 10%. c,d) Plots of the GH shift variation with refractive index of glycerol in distilled water for amorphous HMM (c) and crystalline HMM (d). Numerical fits by transfer matrix method are shown as continuous lines along with experimental results (red dots).

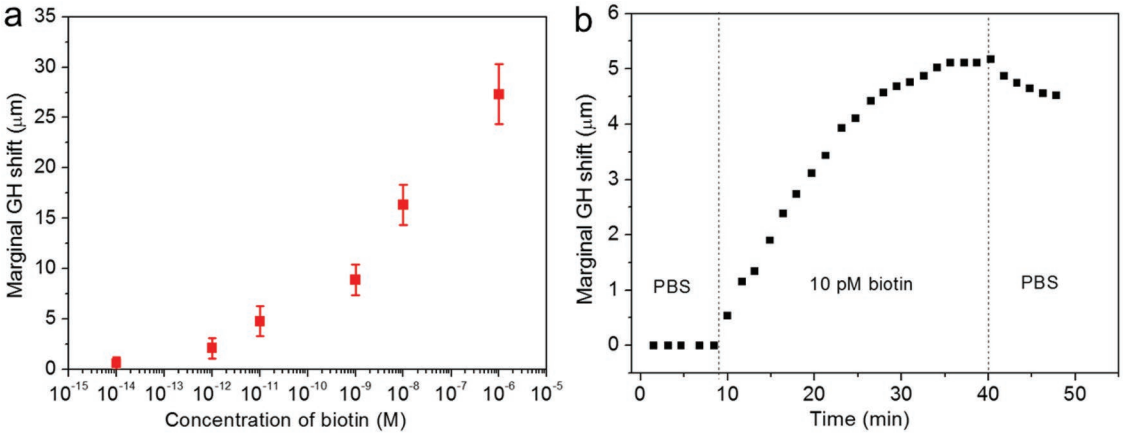

Figure 4. Biosensing based on Goos–Hänchen shift. a) Recorded marginal GH shift after a reaction time of 40 min for different concentrations of biotin in PBS (10×10^{-15} M to 1×10^{-6} M) and b) marginal GH shift change over time with 10×10^{-12} M biotin.

developed a theoretical model to fit the glycerol GH shift data and obtained a very good agreement with experimental results.

This sensor device provides a maximum refractive index sensitivity for the crystalline phase of 13.4×10^{-7} RIU nm^{-1} and a minimum sensitivity for the amorphous phase of 16.3×10^{-7} RIU nm^{-1}. This is because the crystalline phase provides higher phase change at the coupling angle compared to amorphous phase. The GH shift tunability can be further improved by using longer wavelength sources and higher refractive index prisms (see Figure S18, Supporting Information). The calculated bulk refractive index sensitivity of the system is of the order of 10^{-7} RIU nm^{-1} of the shift, which is consistent with experimentally determined sensitivity. The obtained bulk refractive index sensitivity of the proposed HMM is comparable with previously reported systems,[42–48] however, those systems demonstrated enhanced GH shift at NIR wavelengths. Importantly, the proposed low-loss HMM shows enhanced and tunable GH shifts at visible wavelengths, which is useful for the realization of ultrasensitive apta-biosensors based on graphene and HMM.

To demonstrate the capabilities of the proposed sensor for label-free biosensing of small molecules, we initially conducted a proof-of-concept biosensing experiment by detecting lower molecular-weight biomolecules such as D-biotin. We selected biotin as the sensing analyte because it is a model system for small molecule compounds such as vitamins, cancer-specific proteins, hormones, therapeutics, or contaminants. Since gold can be functionalized with biomolecules easily using thiol-based surface chemistry,[53] we first sputtered a 10 nm film of gold on top of the crystalline HMM sample. We then followed the same streptavidin–biotin affinity model protocol used in previous works[16,17] for the capture of biotin.

The experiment was performed in a single injection procedure, in which the refractive index change caused by the capture of biotin at the sensor surface was recorded by measuring the GH shift. In our experiments, initially, GH shift with phosphate buffered saline (PBS) was recorded as a baseline. Then, different concentrations (10×10^{-15} M to 1×10^{-6} M) of biotin prepared in PBS were injected into the sensor channel (sample volume = 98 μL) and the corresponding GH shift with concentration was recorded. The response of the device with time was investigated by calculating the marginal GH shifts ($\delta GH = |GH_{pbs} - GH_{biotin}|$) of different concentrations of biotin. The recorded marginal GH shift after the saturation time (40 min) is shown in **Figure 4**a, which shows an increase in marginal GH shifts with increasing biotin concentrations. The experiments were repeated using different samples and the corresponding error bar was included in the data. In Figure 4b, we plot the marginal GH shift change of a single measurement as the biotin molecules accumulate on the sensor surface over time. A clear step in GH shift with time was recorded. These results indicate an evidence of the binding of biotin molecules to streptavidin sites. By taking into account the experimental noise level, we concluded that the detection limit of the sensor device is less than 1×10^{-12} M. Since it is not straightforward to quantify the exact number of adsorbed biotin molecules responsible for the shift, we estimated the highest number of biotin molecules available at a lowest concentration of 1×10^{-12} M, which is around 11.8×10^5 (see Supporting Information). Note that the extreme refractive index sensitivity due to GH shift interrogation scheme enabled the detection of ultralow molecular weight biomolecules such as biotin at a low concentration of 1×10^{-12} M.

We further propose a label-free plasmonic apta-biosensor platform for thrombin detection. Thrombin is a commonly found enzyme in human blood, therefore the monitoring of thrombin level in blood or plasma is essential for clinical applications. For both research and clinical diagnosis purpose, detection of thrombin is very important because thrombin plays a central role in hemostasis and hemolysis. While different approaches have been demonstrated for thrombin detection at low concentrations,[32,33,54–57] we propose a simple and scalable technique for label-free optical detection of thrombin at ultralow concentrations. Since graphene can selectively adsorb aromatic rings structure biomolecules such as DNA, RNA, peptides, and cytokines through pi-stacking forces[38] and Sb_2S_3–TiN HMM shows enhanced GH shifts at visible wavelengths, the proposed configuration is a unique platform for thrombin detection at ultralow concentrations. In particular, giant enhancement in GH shift at visible wavelength (632.8 nm) compared with HMM alone is possible by using a hybrid platform of graphene and Sb_2S_3–TiN HMM because of the huge field confinement at the graphene–HMM interface.

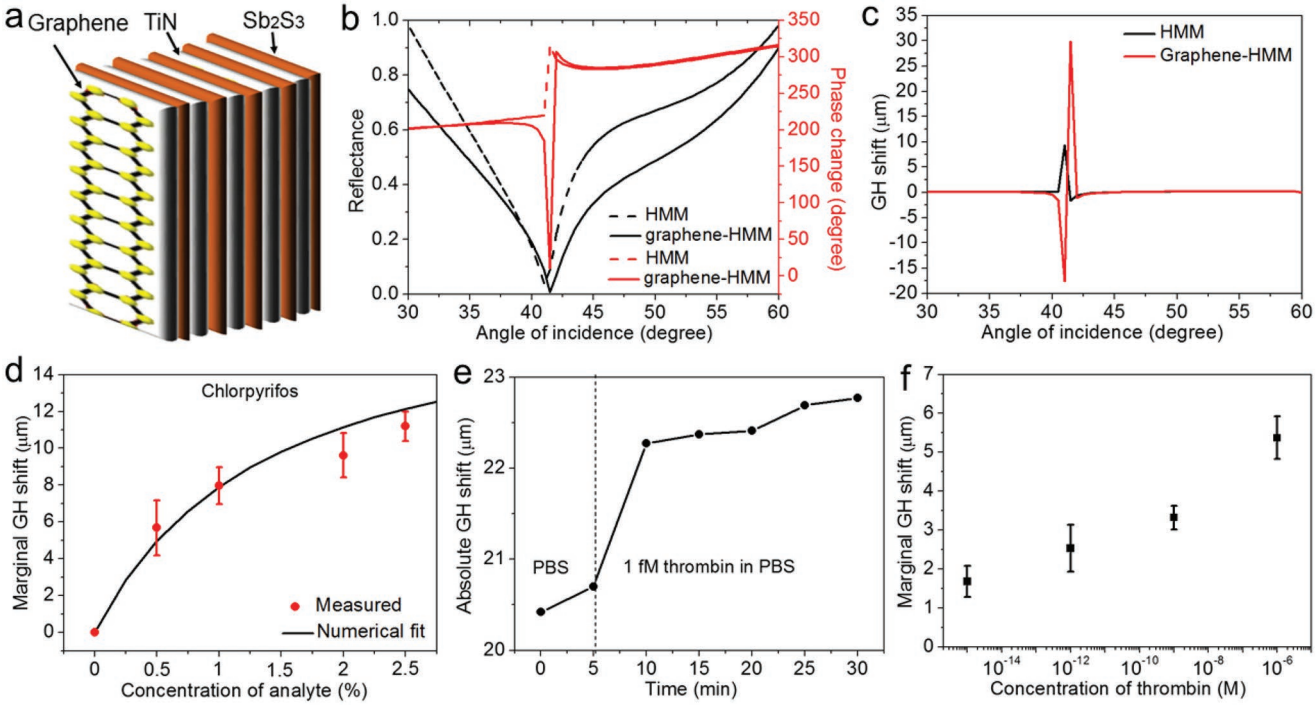

Figure 5. Apta-biosensor platform based on graphene and HMM. a) Schematic of fabricated graphene on Sb_2S_3–TiN HMM sample. b) Calculated reflectance and phase change spectrum of HMM and graphene on HMM. c) Calculated GH shift of HMM and graphene on HMM. d) Measured marginal GH shift with different concentrations of chlorpyrifos. Numerical fits by transfer matrix method are shown as continuous line along with experimental results. e) Measured absolute GH shift over time with 1×10^{-15} M thrombin in PBS. f) Measured marginal GH shift with different concentrations of thrombin in PBS.

A schematic of fabricated apta-biosensor platform based on graphene and Sb_2S_3–TiN HMM is shown in **Figure 5**a. To fabricate the samples, we transferred single layer graphene (SLG) on top of the amorphous Sb_2S_3–TiN HMM. We used CVD method for large-area SLG preparation and single layer of the graphene transferred on the HMM was confirmed by Raman spectroscopy (see Figure S19a, Supporting Information). For both HMM and graphene on HMM, we calculated reflectance and phase change spectra at 632.8 nm wavelength as a function of incident angle, which are shown in Figure 5b. As can be seen, an increase in coupling angle and a reduction in reflected intensity at the coupling angle is obtained for graphene on HMM, as a result the phase change at the coupling angle is drastically increased compared with HMM. We observed similar coupling angle change in our experiments using 632.8 nm wavelength laser (see Figure S19b, Supporting Information). The observed drastic phase change is due to the huge field confinement at the graphene–HMM interface because graphene is a low-loss and high refractive index isotropic dielectric material in the visible wavelengths.[38] In the calculation, the thickness of graphene was set to be 0.5 nm and used refractive index of graphene at 632.8 nm wavelength was obtained from[58] $n_{\text{graphene}} = 3 + i\frac{C_1}{3}\lambda_0$ with C_1 = 5.446 μm^{-1} and λ_0 is the vacuum wavelength. In contrast to HMM, a threefold increase in GH shift is obtained for graphene on HMM due to large phase derivative at the coupling angle, which is shown in Figure 5c.

To experimentally investigate the bulk refractive index sensitivity of graphene on HMM samples, we injected different concentrations (0.5–2.5%w/v) of chlorpyrifos (CPF) prepared in a solvent and recorded the corresponding GH shifts. As shown in Figure 5d, an increase in marginal GH shifts (δGH = $|GH_{solvent} - GH_{CPF}|$) with increasing concentration of CPF is obtained and the measured data points were fitted well with our numerical simulation model based on TMM. A control experiment was also conducted by injecting different concentrations (0.5–2.5%w/v) of lactose (see Figure S20, Supporting Information). We selected lactose as a control because the molar mass of lactose is almost same as that of CPF. It is evident that CPF provided higher GH shifts compared to lactose because CPF has aromatic ring structure, as a result it can easily be adsorbed on the graphene surface through π-stacking forces.

To demonstrate the detection and real-time binding of thrombin at ultralow concentrations, we functionalized graphene on HMM samples with thrombin binding aptamers, TBA (see Supporting Information). Then, different concentrations of thrombin prepared in PBS were injected on the sensor surface (1×10^{-15} M to 1×10^{-6} M) and measured the corresponding GH shifts after a reaction time of 30 min. In Figure 5e, we plot the absolute GH shift change over time (every 5 min) by injecting 1×10^{-15} M thrombin concentration. The raw data of this single measurement as the thrombin molecules accumulate on the sensor surface over time is shown in Figure S21 of the Supporting Information. As shown in Figure 5f, the marginal GH shifts (δGH = $|GH_{pbs} - GH_{thrombin}|$) nonlinearly increase with thrombin concentrations. We also performed control experiments using unfunctionalized samples (see Figure S22, Supporting Information). In contrast to

control sample, a significant change in marginal GH shift with nonlinear response is obtained for TBA functionalized sample when the concentration of thrombin is varied from 1×10^{-15} M to 1×10^{-6} M. As the concentration increases, the possibility of multiple adsorbed molecules leads to interference effects, which resulted in nonlinear response. The observed nonlinear response evidences the specific binding of thrombin on TBA functionalized sample. The detection limit of thrombin achieved using the proposed apta-biosensor is 1×10^{-15} M. The estimated highest number of thrombin molecules on the sensor surface at 1×10^{-15} M concentration is 1180 (see Supporting Information).

To conclude, the applications of noble-metal-based photonic devices are severely limited at visible frequencies due to ohmic losses in metals. In this context, we have experimentally demonstrated a low-loss active HMM for photonic device applications at visible frequencies. Since the interdiffusion of noble metals with chalcogenides due to the direct contact of noble metals and chalcogenides represents a major issue for the practical realization of active photonic devices based on phase change chalcogenides, we proposed a solution to this issue by replacing noble metals with TiN. We have experimentally shown that the excitation of the fundamental guided mode of HMM is possible at visible frequency using the prism coupling scheme due to the type-I nature of Sb_2S_3–TiN HMM. We further demonstrated that refractometric sensing is possible using the proposed HMM, by excitation the guided mode of HMM using prism coupling technique and employing GH shift interrogation scheme. The proposed sensor device provided tunable sensitivity with a maximum for crystalline phase and minimum for amorphous phase. Therefore, the tunable differential response of our sensor offers a promising opportunity to design an assay for the selective detection of higher- and lower-molecular-weight biomolecules. In particular, a tunable biosensor device can be developed using this configuration so that the sensitivity of the device can be tuned by electrically or optically.[37] Even though, an electrically tunable graphene-based plasmonic biosensor operates in the mid-infrared frequencies has been demonstrated for the specific label-free detection of protein monolayers,[59] the proposed active HMM can be used to develop tunable plasmonic biosensors in the visible frequencies. We demonstrated the detection and real-time binding of small molecules such as biotin at 1×10^{-12} M concentration. Since HMM improved the detection limit of small biomolecules and aptamers have the capability to detect small biomolecules, we have further demonstrated a plasmonic apta-biosensor based on a hybrid platform of graphene and HMM and detected thrombin concentration as low as 1×10^{-15} M. The proposed apta-sensor platform could be useful for commercial biosensing applications since the prism-coupled SPR-based biosensor platform is already commercialized. In addition, the GH shift tunability of the proposed sensors can be further improved by using high refractive index prisms and a suitable excitation source wavelength. Visible wavelength source is important for the proposed biosensor platforms because the low-loss Sb_2S_3–TiN HMM shows maximum tunability in the visible wavelengths as well as the maximum field confinement at graphene–HMM interface is possible at visible wavelengths due to the high refractive index of graphene. Even though prism is a bulky component, prism coupling enabled angular scan is highly advantageous since a single wavelength visible laser source can be used rather than polychromatic light. Therefore, it is possible to achieve higher signal-to-noise ratio owing to the wavelength and power stability of the source, which gives higher measurement precision.

Supporting Information

Supporting Information is available from the Wiley Online Library or from the author.

Acknowledgements

The authors (K.V.S. and R.S.) acknowledge Singapore Ministry of Education (MOE) (Grant No. MOE2015-T2-2-103) for funding of this research. S.S. and C.T.L. acknowledge support from the NUS-Biomedical Institute for Global Health Research and Technology. We thank Dr. Giorgio Adamo (CDPT, NTU-Singapore) for his support with SEM imaging.

Conflict of Interest

The authors declare no conflict of interest.

Keywords

Goos–Hänchen shift, hyperbolic metamaterials, label-free biosensing, phase change chalcogenides, visible frequencies

Received: January 14, 2019
Revised: March 15, 2019
Published online:

[1] A. Poddubny, I. Iorsh, P. Belov, Y. Kivshar, *Nat. Photonics* **2013**, *7*, 948.
[2] J. Schilling, *Phys. Rev. E* **2006**, *74*, 046618.
[3] I. Avrutsky, I. Salakhutdinov, J. Elser, V. Podolskiy, *Phys. Rev. B* **2007**, *75*, 241402.
[4] K. V. Sreekanth, A. De Luca, G. Strangi, *Sci. Rep.* **2013**, *3*, 3291.
[5] K. V. Sreekanth, A. De Luca, G. Strangi, *J. Opt.* **2014**, *16*, 105103.
[6] A. J. Hoffman, L. Alekseyev, S. S. Howard, K. J. Franz, D. Wasserman, V. A. Podolskiy, E. E. Narimanov, D. L. Sivco, C. Gmachl, *Nat. Mater.* **2007**, *6*, 946.
[7] K. V. Sreekanth, A. De Luca, G. Strangi, *Appl. Phys. Lett.* **2013**, *103*, 023107.
[8] A. A. Govyadinov, V. A. Podolskiy, *Phys. Rev. B* **2006**, *73*, 155108.
[9] H. N. S. Krishnamoorthy, Z. Jacob, E. Narimanov, I. Kretzschmar, V. M. Menon, *Science* **2012**, *336*, 205.
[10] K. V. Sreekanth, K. Hari Krishna, A. De Luca, G. Strangi, *Sci. Rep.* **2015**, *4*, 6340.
[11] V. Caligiuri, R. Dhama, K. V. Sreekanth, G. Strangi, A. De Luca, *Sci. Rep.* **2016**, *6*, 20002.
[12] M. Y. Shalaginov, J. Liu, M. Ferrera, A. V. Akimov, A. Lagutchev, A. N. Smolyaninov, V. V. Klimov, J. Irudayaraj, A. V. Kildishev, A. Boltasseva, V. M. Shalaev, *Laser Photonics Rev.* **2015**, *9*, 120.

[13] K. V. Sreekanth, M. ElKabbash, Y. Alapan, A. R. Rashed, U. A. Gurkan, G. Strangi, *Sci. Rep.* **2016**, *6*, 26272.
[14] Y. Guo, Z. Jacob, *Opt. Express* **2013**, *21*, 15014.
[15] A. V. Kabashin, P. Evans, S. Pastkovsky, W. Hendren, G. A. Wurtz, R. Atkinson, R. Pollard, V. A. Podolskiy, A. V. Zayats, *Nat. Mater.* **2009**, *8*, 867.
[16] K. V. Sreekanth, Y. Alapan, M. ElKabbash, E. Ilker, M. Hinczewski, U. A. Gurkan, A. De Luca, G. Strangi, *Nat. Mater.* **2016**, *15*, 621.
[17] K. V. Sreekanth, Y. Alapan, M. ElKabbash, A. M. Wen, E. Ilker, M. Hinczewski, U. A. Gurkan, N. F. Steinmetz, G. Strangi, *Adv. Opt. Mater.* **2016**, *4*, 1659.
[18] F. L. Liu, L. Xiao, Y. Ye, M. Wang, K. Cui, X. Feng, W. Zhang, Y. Huang, *Nat. Photonics* **2017**, *11*, 289.
[19] G. V. Naik, J. L. Schroeder, X. Ni, A. V. Kildishev, T. D. Sands, A. Boltasseva, *Opt. Mater. Express* **2012**, *2*, 478.
[20] G. V. Naik, B. Saha, J. Liu, S. M. Saber, E. A. Stach, J. M. K. Irudayaraj, T. D. Sanda, V. M. Shalaev, A. Boltasseva, *Proc. Natl. Acad. Sci. USA* **2014**, *111*, 7546.
[21] Y. C. Chang, C. H. Liu, C. H. Liu, S. Zhang, S. R. Marder, E. E. Narimanov, Z. Zhong, T. B. Norris, *Nat. Commun.* **2016**, *7*, 10568.
[22] J. S. Wu, D. N. Basov, M. M. Fogler, *Phys. Rev. B* **2015**, *92*, 205430.
[23] S. Dai, Q. Ma, M. K. Liu, T. Andersen, Z. Fei, M. D. Goldflam, M. Wagner, K. Watanabe, T. Taniguchi, M. Thiemens, F. Keilmann, G. C. A. M. Janssen, S.-E. Zhu, P. Jarillo-Herrero, M. M. Fogler, D. N. Basov, *Nat. Nanotechnol.* **2015**, *10*, 682.
[24] J. D. Caldwell, Y. Chen, V. Giannini, M. M. Fogler, Y. Francescato, C. T. Ellis, J. G. Tischler, C. R. Woods, A. J. Giles, M. Hong, K. Watanabe, T. Taniguchi, S. A. Maier, K. S. Novoselov, *Nat. Commun.* **2014**, *5*, 5221.
[25] H. N. S. Krishnamoorthy, Y. Zhou, S. Ramanathan, E. Narimanov, V. M. Menon, *Appl. Phys. Lett.* **2014**, *104*, 121101.
[26] S. Prayakarao, B. Mendoza, A. Devine, C. Kyaw, R. B. Van Dover, M. A. Nogino, *Appl. Phys. Lett.* **2016**, *109*, 061105.
[27] H. N. S. Krishnamoorthy, B. Gholipour, N. I. Zheludev, C. Soci, *Adv. Opt. Mater.* **2018**, *6*, 1800332.
[28] L. Bardotti, P. Jensen, A. Hoareau, M. Treilleux, B. Cabaud, A. Perez, F. Cadete Santos Aires, *Surf. Sci.* **1996**, *367*, 276.
[29] M. Mitkova, M. N. Kozicki, H. C. Kim, T. L. Alford, *Thin Solid Films* **2004**, *449*, 248.
[30] J. Ping, Y. Zhou, Y. Wu, V. Papper, S. Boujday, R. S. Marks, T. W. J. Steele, *Biosens. Bioelectron.* **2015**, *64*, 373.
[31] B. N. Shivananju, W. Yu, Y. Liu, B. Lin, S. Li, Q. Bao, *Adv. Funct. Mater.* **2017**, *27*, 1603918.
[32] S. Wang, S. Bi, Z. Wang, J. Xia, F. Zhang, M. Yang, R. Gui, Y. Li, Y. Xia, *Chem. Commun.* **2015**, *51*, 7927.
[33] Y. Wang, Y. Xiao, X. Ma, N. Li, X. Yang, *Chem. Commun.* **2012**, *48*, 738.
[34] Q. Wang, E. T. F. Rogers, B. Gholipour, C. M. Wang, G. Yuan, J. Teng, N. I. Zheludev, *Nat. Photonics* **2016**, *10*, 60.
[35] L. Lu, W. Dong, J. K. Behera, L. Chew, R. E. Simpson, *J. Mater. Sci.* **2019**, *54*, 2814.
[36] M. Y. Versavel, J. A. Haber, *Thin Solid Films* **2007**, *515*, 7171.
[37] W. Dong, H. Liu, J. K. Behera, L. Lu, R. J. H. Ng, K. V. Sreekanth, X. Zhou, J. K. W. Yang, R. E. Simpson, *Adv. Funct. Mater.* **2019**, *29*, 1806181.
[38] S. Zeng, K. V. Sreekanth, J. Shang, T. Yu, F. Yin, D. Baillargeat, P. Coquet, H. P. Ho, A. V. Kabashin, K. T. Yong, *Adv. Mater.* **2015**, *27*, 6163.
[39] F. Goos, H. Hanchen, *Ann. Phys.* **1947**, *436*, 333.
[40] R. Yang, W. Zhu, J. Li, *Opt. Express* **2014**, *22*, 2043.
[41] E. Pfleghaar, A. Marseille, A. Weis, *Phys. Rev. Lett.* **1993**, *70*, 2281.
[42] Y. Wan, Z. Zheng, W. Kong, X. Zhao, Y. Liu, Y. Bian, J. Liu, *Opt. Express* **2012**, *20*, 8998.
[43] P. R. Berman, *Phys. Rev. E* **2002**, *66*, 067603.
[44] L. Luo, T. Tang, *Superlattices Microstruct.* **2016**, *94*, 85.
[45] C. W. Chen, T. Bian, H. P. Chiang, P. T. Leung, *J. Opt.* **2016**, *18*, 025104.
[46] J. Zhao, H. Zhang, X. Zhang, D. Li, H. Lu, M. Xu, *Photonics Res.* **2013**, *1*, 160.
[47] C. Xu, J. Xu, G. Song, C. Zhu, Y. Yang, G. S. Agarwal, *Opt. Express* **2016**, *24*, 21767.
[48] X. Yin, L. Hesselink, *Appl. Phys. Lett.* **2006**, *89*, 261108.
[49] X. Liu, Z. Cao, P. Zhu, Q. Shen, X. Liu, *Phys. Rev. E* **2006**, *73*, 056617.
[50] X. Wang, M. Sang, W. Yuan, Y. Nie, H. Luo, *IEEE Photonics Technol. Lett.* **2016**, *28*, 264.
[51] K. V. Sreekanth, W. Dong, Q. Ouyang, S. Sreejith, M. ElKabbash, C. T. Lim, G. Strangi, K. T. Yong, R. E. Simpson, R. Singh, *ACS Appl. Mater. Interfaces* **2018**, *10*, 34991.
[52] K. V. Sreekanth, Q. Ouyang, S. Han, K. T. Yong, R. Singh, *Appl. Phys. Lett.* **2018**, *112*, 161109.
[53] P. Baptista, E. Pereira, P. Eaton, G. Doria, A. Miranda, I. Gomes, P. Quaresma, R. Franco, *Anal. Bioanal. Chem.* **2008**, *391*, 943.
[54] G. Shen, H. Zhang, C. Yang, Q. Yang, Y. Tang, *Anal. Chem.* **2017**, *89*, 548 .
[55] Q. Xu, G. Wang, M. Zhang, G. Xu, J. Lin, X. Luo, *Microchim. Acta* **2018**, *185*, 253.
[56] Y. Niu, M. Chu, P. Xu, S. Meng, Q. Zhou, W. Zhao, B. Zhao, J. She, *Biosens. Bioelectron.* **2018**, *101*, 174.
[57] H. Kim, Z. An, C. H. Jang, *Microchem. J.* **2018**, *141*, 71.
[58] M. Bruna, S. Borini, *Appl. Phys. Lett.* **2009**, *94*, 031901.
[59] D. Rodrigo, O. Limaj, D. Janner, D. Etezadi, F. J. G. de Abajo, V. Pruneri, H. Altug, *Science* **2015**, *349*, 165.